

Dynamic response tuning of composite beams by embedded shape memory alloy actuators

Travis L. Turner*

NASA Langley Research Center, MS 463
Hampton, VA 23681-2199

1. ABSTRACT

The thermomechanical performance of a shape memory alloy hybrid composite beam specimen is demonstrated and used in a preliminary validation study of a recently developed constitutive model and finite element formulation for analysis of such structures. A brief description of the thermoelastic formulation is given. A material system consisting of a glass/epoxy matrix with embedded Nitinol actuators was chosen for this study. Results from Nitinol material characterization testing, beam specimen fabrication processes, and base acceleration testing for measuring the dynamic response performance is presented. Selected results from the dynamic tests are shown, interpreted, and compared with predictions from the FE model. Elimination of a thermal post-buckling deflection by the activated SMA was observed. The fundamental natural frequency is shown to increase by a factor of 5.3 and the RMS displacement response is attenuated by a factor 6.4. Preliminary comparisons between predicted and measured performance is good. Discrepancies are attributable to insufficient knowledge of the matrix material properties at elevated temperature.

Keywords: Shape Memory Alloys, Nitinol, Hybrid Composites, Thermoelasticity, Constitutive Modeling, Finite Element Analysis, Material Nonlinearity, Thermal Buckling, Thermal Post-Buckling, Random Response

2. INTRODUCTION

Excitation levels for many aerospace vehicle structures are high due to engine noise and turbulent boundary layer fluctuating pressures. The ever-increasing need for weight-efficient structures in these applications leads to significant sonic fatigue and interior noise issues. Conventional aerospace structures typically employ passive treatments such as structural stiffening, constrained layer damping, and acoustic absorption materials to reduce the structural response and interior acoustic levels. These treatments suffer from substantial weight penalty and are often limited to relatively low temperatures and/or high frequencies. Smart materials may enable new structural design paradigms for high performance, durable structures. There are many smart materials concepts, but some involving shape memory alloys (SMAs) appear to have significant advantages for applications involving adaptive stiffening and structural shape control.

Shape memory alloys are a class of smart materials that exhibit a martensitic phase transformation when cooled through the transformation temperature range $M_s \rightarrow M_f$ from the high temperature austenitic state, see Figure 1. The interaction of temperature and applied stress in driving the martensitic and reverse transformations can be used to exploit phenomena such as the shape memory effect (SME) and pseudo-elasticity. The SME can be described in simple terms in the following manner. A SMA can be easily deformed in the low temperature martensitic condition and can be returned to its original configuration by heating through the reverse transformation temperature range $A_s \rightarrow A_f$. This type of SME is termed free recovery. Conversely, in a constrained recovery configuration, the SMA is prevented from recovering the initial strain and a large tensile stress (recovery stress) is induced. A situation in which the specimen performs work (deforms under load) is called restrained recovery. Extensive work has been done to characterize these materials, both qualitatively through theoretical models¹⁻⁴ and quantitatively for particular alloys^{5,6}. Compilations of papers have also been published, most recently by Otsuka and Wayman⁷. Birman⁸ gave a review of work done in the areas of alloy characterization, constitutive modeling, and applications.

Although there are several alloy systems that exhibit the shape memory effect, Nitinol has the most engineering significance. The name for this family of alloys was derived from Nickel, Titanium, and Naval Ordnance Laboratory and was patented by Buehler and Wiley⁹. The SME for this family of alloys is limited to nearly equiatomic compositions; Nickel content from 53 to 57 percent by weight. Advantages include ductility at low temperature, high degree of shape recovery capability, large pseudoelastic hysteresis, corrosion and fatigue resistance, biomedical compatibility, and relatively high electrical resistance.

* Email: t.l.turner@larc.nasa.gov, Phone: 757-864-3598, Fax: 757-864-8823

Shape memory alloys have been investigated for a variety of applications since their discovery^{10–13}. The concept of embedding SMA actuators in a composite laminate, termed a shape memory alloy hybrid composite (SMAHC), was introduced by Rogers and Robertshaw¹⁴. Subsequent studies considered SMA actuators, external to the structure, for active vibration control^{15–17} and shape control¹⁸ of cantilevered beams. Other studies have proposed SMA actuators for vibration control of space structures¹⁹ and presented analytical formulations to demonstrate the vibration/structural acoustic control of SMAHC panels^{20,21}. Studies of thermal post-buckling²² and random dynamic response²³ suppression of SMAHC panels were presented using a thermoelastic FE formulation. A different approach was offered by Ro and Baz^{24–26}, where thermal, static, and dynamic analyses were developed for the case of SMA actuators passing through sleeves in composite plates. Birman²⁷ investigated optimal distributions of SMA actuators in sleeves to improve the buckling performance of sandwich panels under mechanical loading.

SMAHC structures incorporating prestrained actuators are of particular interest in this study because of the potential for structural control due to tensile recovery stresses that are generated (constrained recovery) when the structure is placed in its service environment. In this way, an inherently elevated temperature (e.g. many aerospace applications) can be used to control structural response without control electronics or auxiliary power. There is a need for an analytical tool that accurately predicts the mechanics of SMAHC structures with embedded, bonded actuators, which offer unique advantages for structural control. The purpose of the present work is to present progress on an experimental program to demonstrate control over the dynamic response of SMAHC structures and to validate a recently developed FE analysis for prediction of the thermomechanical response of SMAHC structures.

3. MODEL FORMULATION

3.1 Constitutive Modeling

Constitutive theories for SMAHC structures can be developed from the previously mentioned shape memory models^{1–4}, as was done by Boyd and Lagoudas²⁸ and Birman²⁹. However, these models are difficult to use in practice. An alternative approach is to employ a constitutive model which makes use of experimental measurement of fundamental engineering properties. A new model of the latter type was recently developed by Turner³⁰. This model casts the uniaxial thermoelastic constitutive relation for a SMA actuator, along the axis of the actuator, in terms of an effective coefficient of thermal expansion (CTE):

$$\sigma_{1a} = E_a \left[\epsilon_1 - \int_{T_o}^T \alpha_{1a}(\tau) d\tau \right] \quad (1)$$

where E_a is the Young's modulus of the SMA, ϵ_1 is the mechanical strain in the 1-direction, and α_{1a} is the “effective” (nonlinear) CTE. Note that this expression is valid for constrained, restrained, or free recovery applications; only the empirical method of obtaining the thermal strain changes. A measure of the nonlinear CTE $\alpha_{1a}(T)$ over the temperature range of concern would be appropriate for free or restrained recovery applications. For constrained recovery applications, however, one must resort to measurement of the recovery stress and modulus.

It can be shown that, for constrained recovery behavior, the nonlinear thermal strain in Equation (1) can be modeled by linear thermal expansion below the austenite start temperature and can be related to the SMA recovery stress σ_r and modulus by the equation

$$\sigma_r = -E_a \int_{T_0}^T \alpha_{1a}(\tau) d\tau \quad \text{or} \quad \int_{T_0}^T \alpha_{1a}(\tau) d\tau = -\frac{\sigma_r}{E_a} \quad (2)$$

at temperatures above A_s . Note that in this case, the nonlinear thermoelastic nature of the SMA is still captured, albeit in a different way, because measurements of recovery stress and modulus versus temperature are inherently cumulative (integrated). Also, note that an experimental approach could be devised to measure appropriate recovery stress σ_r quantities for restrained recovery applications as an alternative to direct measurement of $\alpha_{1a}(T)$. The uniaxial SMA constitutive relation for the transverse direction has a form analogous to Equation (1). However, $\alpha_{2a}(T)$ is not related to the recovery stress, but is nonlinear due to the differing martensitic and austenitic properties. This constitutive model will be referred to as the effective coefficient of thermal expansion (ECTE) model.

3.2 Governing Equations

The ECTE constitutive model for the SMA was used in a rule of mixtures approach to develop the thermoelastic constitutive relations for a thin orthotropic SMAHC lamina under conditions of plane stress. These constitutive relations, along with the von Kármán strain-displacement relations, were used as a variational principle to derive the equations governing the thermomechanical response of a SMAHC panel-type structure subjected to combined steady-state thermal and out-of-plane, dynamic, mechanical loads. The resulting finite element system of equations can be written in the following form

$$\begin{bmatrix} M_b & 0 \\ 0 & M_m \end{bmatrix} \begin{Bmatrix} \ddot{A}_b \\ \ddot{A}_m \end{Bmatrix} + \left(\begin{bmatrix} K_b & K_B \\ K_B^T & K_m \end{bmatrix} - \begin{bmatrix} K_{\Delta T} & 0 \\ 0 & 0 \end{bmatrix} + \frac{1}{2} \begin{bmatrix} N1_b + (N1_b)_B & N1_{bm} \\ N1_{mb} & 0 \end{bmatrix} + \frac{1}{3} \begin{bmatrix} N2_b & 0 \\ 0 & 0 \end{bmatrix} \right) \begin{Bmatrix} A_b \\ A_m \end{Bmatrix} = \begin{Bmatrix} F_b(t) \\ 0 \end{Bmatrix} + \begin{Bmatrix} P_{b\Delta T} \\ P_{m\Delta T} \end{Bmatrix} \quad (3)$$

or

$$[M] \{ \ddot{A} \} + ([K] - [K_{\Delta T}] + \frac{1}{2}[N1] + \frac{1}{3}[N2]) \{ A \} = \{ F(t) \} + \{ P_{\Delta T} \} \quad (4)$$

where $[M]$ and $[K]$ are the usual system mass and linear stiffness matrices; $[K_{\Delta T}]$ is the geometric stiffness matrix due to the thermal in-plane force vector $\{N_{\Delta T}\}$; $[N1]$ and $[N2]$ are the first- and second-order nonlinear stiffness matrices which depend linearly and quadratically upon displacement $\{A\}$, respectively; $\{F(t)\}$ is the mechanical excitation load vector, and $\{P_{\Delta T}\}$ is the thermal force vector. The subscripts b and m denote bending and membrane components, respectively, and the subscript B indicates that the corresponding stiffness matrix is due to the laminate bending-membrane coupling stiffness matrix $[B]$. Note that the stiffness matrices $[K]$, $[K_{\Delta T}]$, $[N1]$, $[N2]$ and the thermal force vector $\{P_{\Delta T}\}$ are all temperature dependent.

Three types of analyses are required to study the response of structures to thermal and dynamic mechanical loads, governed by Equations (4): (1) thermal buckling analysis, (2) thermal post-buckling analysis, and (3) dynamic analysis. Details of the constitutive model, FE formulation, and solution procedures can be found in Turner³⁰.

4. MATERIAL SYSTEM CHARACTERIZATION

In the typical application being considered, the SMA elements would be activated through an inherently elevated temperature of the service environment. This effect can be simulated in experiments by electrically activating the SMA through resistive heating. This method has the advantages of simple operation, relatively uniform heating, and excellent controllability. A glass/epoxy matrix material system was selected to avoid any potential electrical conduction problems. This material system also affords the advantage of visual flaw detection. The resin for this material system is formulated for autoclave processing with a 176.67°C (350°F) cure. Nominal mechanical properties for the material system are given in Table 1.

Most recent SMAHC structural designs have focused on SMA wire-type actuators distributed uniformly throughout the laminate or individual laminae. The present work focuses on SMA hybrid composite laminates involving ribbon-type SMA actuators to simplify the fabrication procedure, allow for more flexibility in fabrication, and desensitize the actuators to interface voids and stress concentrations. For example, the ribbon-type SMA elements can be placed in strips cut out of specific matrix laminae to result in a rather simple lay-up operation, while keeping the volume fraction high in desired locations. Another potential benefit of this type of lay-up procedure is that it could potentially be extended directly to e-beam consolidation procedures where spools of SMA ribbon would strategically replace spools of matrix material ribbon.

Nitinol ribbon material was procured with a cross section of 0.090×0.006 inches. The transformation temperatures for the alloy in a fully annealed state were reported by the vendor as $A_s=67^\circ\text{C}$, $A_f=85^\circ\text{C}$, $M_s=46^\circ\text{C}$, and $M_f=32^\circ\text{C}$. Note that this gives a martensite finish temperature above the expected ambient temperature while maintaining an austenite finish temperature well below the cure temperature of the epoxy matrix. These temperatures were reportedly determined by differential scanning calorimetry (DSC). It was expected that mechanical constraints in the planned tests would increase the phase transformation temperatures. However, the provided material is not in a fully annealed state, so it was also expected that the transformation temperatures would be lowered by remaining dislocations. DSC tests were performed on samples of the provided material to determine the baseline phase transformation temperatures.

Small samples (<10mg) were cut from the ribbon in the as-received condition for the DSC testing. Scans were performed at a rate of 5°C/minute with the following procedure; heat from ambient temperature to 150°C (*first heat*), cool

from 150°C to -20°C, and repeating this entire profile once the sample was returned to ambient from -20°C (*second heat*). Representative results from the DSC tests are shown in Figure 2. The shape of the first-heat endotherms were ill-behaved and not repeatable, while the analogous second-heat endotherms were repeatable. This is attributable to first-heat recovery of the mechanical deformation induced by shearing small DSC samples from longer lengths. Note that the DSC signatures show two exothermic peaks during the cooling portion of the cycles; one peaking at approximately 39°C and attributable to a R-phase transformation, the other peaking at approximately 9°C due to the usual twinned martensitic transformation. The R-phase is a by-product of a partially annealed condition and does not adversely affect performance, see Otsuka and Wayman⁷. Thus, the transformation temperatures for the Nitinol in the as-received condition and in a free configuration are approximately $A_s=45^\circ\text{C}$, $A_f=60^\circ\text{C}$, $M_s=17^\circ\text{C}$, and $M_f=0^\circ\text{C}$. The DSC results give significant insight into the state of the alloy, but mechanical properties are needed to model the behavior of the material.

Data pertaining to the material property and performance characteristics of the alloy were acquired through mechanical testing performed by Lockheed Martin Astronautics, see Draper³¹. Although rigorous training could have been performed on the alloy to generate a thermomechanically stable actuator material, the cure temperature associated with the glass-epoxy matrix material (350°F) was considered to be high enough to risk degrading the expensive training. Thus, thermomechanical tests were performed to quantify the material characteristics as a function of thermal cycle. Isolength (constant strain) and isothermal tests were performed on nominally 10-inch lengths of the material.

Isolength tests were performed to measure the maximum recovery stress generated by the actuator material as a function of cycle and initial strain (2%, 3%, and 4%). In all cases, the recovery stress diminished rapidly out to about 10 thermal cycles and approached an asymptotic value at 50 cycles. Additional isolength tests were performed with the 2% and 4% prestrain samples after the thermal cycling tests to measure the variation of the stabilized recovery stress with temperature. An estimate of the variation of recovery stress with thermal cycle number and temperature was calculated by normalizing the recovery stress versus temperature data to the corresponding maximum recovery stress versus cycle data. The resulting carpet plot for the 4% prestrain case is shown in Figure 3. This allows modeling of the material system without any requirement on thermal cycling of SMAHC specimens. Although it cannot be seen in the plot, mechanical constraint shifted the martensitic transformation temperatures above ambient temperature, as evidenced by the recovery stress returning to zero at approximately 46°C (115°F).

Isothermal tests were conducted to measure load versus deflection for all specimens, as well as a specimen in the as-received condition, at ambient and elevated temperature (120°C). Ambient Young's modulus estimates were calculated from only the initial (0–8.9 N, 0–2 lbf applied load) portion of the ambient temperature curve, while the overall slope of the elevated temperature data was used for hot Young's modulus estimates. The resulting modulus data and values summarizing the isolength testing for all of the samples is shown in Table 2. The Nitinol material properties are summarized in Table 1.

5. SPECIMEN FABRICATION AND EXPERIMENTAL APPARATUS

The previously described FE formulation was used to design candidate specimens for performance demonstration and experimental validation of the analytical tool. Numerical results, along with test hardware and other constraints, led to the beam specimen design shown schematically in Figure 4. The specimen design is by no means optimized, but the predicted performance is in a range that is suitable for the expected loading conditions and to demonstrate significant improvement from the SMA reinforcement. A tooling plate for lay-up and cure of these specimens was designed with knurled clamping restraints at the boundaries to prevent prestrain recovery during cure.

Lengths (0.635 m, 25 in) of the SMA ribbon were prestrained 4% (elongated to 0.6604 m, 26 in) in a mechanical testing machine prior to laminate fabrication. Five actuators were laid side-by-side in strips cut out of the 0° layers to develop the half-inch width (actually 0.45-in) in the specimen design. The ends of the actuators were clamped in the tooling plate and the entire assembly was vacuum-bagged for autoclave cure. Beam specimens were machined from the laminate resulting from this lay-up and cure procedure. The beam dimensions are 0.5588x0.0254x0.0019 m (22x1x0.076 in). The SMA leads were trimmed to an overall length of 0.6604 m (26 in). The overall volume fraction of the SMA within the glass/epoxy dimensions is approximately 14%. The beam mass was calculated from the material properties in Table 1 to be 0.0741 kg, which is within 1% of the measured mass (0.0749 kg).

Experiments were conducted with a SMAHC beam in the Test and Development Branch, Vibration Lab at NASA Langley Research Center. The apparatus consists of a large electromechanical shaker, which drives a magnesium slip table in a horizontal plane. Pictures of the beam specimen installed in a support fixture and of the overall base excitation experimental setup are shown in Figure 5. The beam has an unsupported length of 0.4572 m (18 in) within the mechanical

grips. The SMA leads are clamped in separate grips for mechanical constraint and electrical connection. The mechanical and electrical grips are indicated in the figure by the symbols “m” and “e”, respectively. The beam/electrical connections are thermally/electrically isolated from the fixture by a layer of fibrous ceramic insulation. The beam is heated by DC electrical current controlled by a thermocouple measurement located approximately on the beam centerline and 0.0127 m (0.5 in) from the right mechanical grip. Thermocouples are also attached to each end of the fixture and one measures the ambient air temperature. The two-dimensional temperature distribution on the beam is sensed by an infrared thermal imaging camera.

The beam/fixture assembly is attached to the slip table such that the beam-width is oriented in the vertical direction to allow the shaker to drive out-of-plane motion in the beam without the effects of gravity. The base acceleration is controlled by accelerometers attached to each end of the fixture. The beam is instrumented with two accelerometers; one at 0.1016 m (4 in) and the other at 0.254 m (10 in) from the left mechanical grip. These locations will be referred to as locations 1 and 2 as indicated in Figure 5. The beam response is also measured by a laser vibrometer aimed at location 2. The previously described FE analysis predicts relative motion for base acceleration excitation, as do most such analyses, so relative responses must be constructed from absolute measurements. This was accomplished for the laser velocity data by performing hardware integration on two redundant accelerometers attached to the fixture.

6. RESULTS AND DISCUSSION

The beam was excited by random base acceleration over a 10–400 Hz bandwidth with a RMS value of 0.25 g. Time records with an overall length of 200 seconds were collected with a sampling rate of 1024 Hz to allow 50–frame averages with a bandwidth of 0–400 Hz and a frequency resolution of 0.25 Hz. The time data was post-processed to construct relative response quantities, frequency response functions between the beam response transducers and the fixture transducers, and power spectral densities (PSDs) of the acceleration input and relative beam responses. Dynamic data was collected at ambient and at elevated temperatures from 32.22°C (90°F) to 121.11°C (250°F) in 5.56°C (10°F) increments. The beam mechanical and ribbon electrical grips were torqued to 13.56 N•m (120 in•lbf) just prior to dynamic excitation to minimize effects of changing environmental conditions. The fixture temperature increased by approximately 2.22°C (4°F) during the course of data collection, which was in almost direct proportion to the increase in ambient air temperature.

Some interesting qualitative results were observed during data collection. The beam had a noticeable thermal post-buckling deflection even at the 32.22°C (90°F) level. At 48.89°C (120°F), the deflection was quite large. However, upon raising the temperature to 54.44 °C (130 °F), a thermal post-buckling deflection was no longer discernible. This behavior is attributable to the fact that the specific alloy used in this case has a A_s greater than ambient, see Turner (2000). The forced vibration amplitude was visually noticeable in the inactive state (ambient temperature), but was virtually undetectable at temperatures above 71.11°C (160°F). No evidence of delamination or other flaws were detected subsequent to testing, despite the large thermal post-buckling deflection and rather high temperature developed during the tests.

Other observations can be made from a summary of RMS displacement responses and modal parameter estimates shown as a function of temperature in Table 3. Temperatures for which the beam was buckled are excluded from the table. The RMS displacements correspond to location 2 and were calculated in the frequency domain from the corresponding accelerometer PSDs. It can be seen that, although a majority of the stiffening effect was achieved at approximately 71.11°C (200°F), performance remains good far beyond that temperature with a maximum increase in the fundamental frequency of 430% at 121.11°C (250°F). Note the peculiar changes in the mode–1 damping near 71.11°C (160°F). One possible explanation is that there may be adequate austenite and dynamic stress to enhance damping by stress induced martensitic (SIM) transformation hysteresis. At higher temperatures, the dynamic stresses are insufficient to drive the SIM transformation as it becomes increasingly difficult to induce. This damping mechanism is reflected in the RMS displacement response data, where it can be seen that the displacement response increases at 76.67°C (170°F). These effects are perhaps more easily seen in comparing the displacement response PSDs for location 2 at four temperatures, see Figure 6.

A FE model of this system was developed for the purposes of validation. The beam was modeled with a 36x2 mesh of 24 degree-of-freedom rectangular plate elements. Element properties were constructed from the glass/epoxy and Nitinol material properties given in Table 1. The boundary conditions were modeled as clamped with the exception of adjustable torsional springs applied to the longitudinal-slope degrees of freedom at the mechanical grips. Modal damping estimates from measured frequency response functions, see Table 3, were also used in the predictions. The influence of the accelerometers was modeled as lumped masses. The temperature distribution was taken to be uniform, which is fairly accurate as evidenced by the thermal imaging data. The input acceleration PSDs, as measured by one of the control accelerometers, was taken as input for the predictions. Comparisons between predicted and measured displacement PSDs for location 2 at ambient

temperature and 71.11°C (160°F) are shown in Figure 7. The comparison at ambient temperature is excellent, but there is some discrepancy at 71.11°C (160°F). It can be seen that the discrepancy diminishes with temperature as shown in Figure 8, which shows the same comparison at 93.33°C (200°F). Note that the elevated temperature predictions were made with nominal, ambient temperature glass/epoxy material properties. This trend is probably caused by an underestimation of the longitudinal matrix CTE and overestimation of the elevated temperature matrix moduli. Changes in these parameters in the indicated directions would improve the comparison. Work is currently in progress to measure the full complement of matrix material properties and perform a rigorous correlation with experimental results.

7. CONCLUSIONS

Two main objectives of this work are to demonstrate control over the dynamic response of SMAHC beams and to validate a recently developed constitutive and finite element formulation for prediction of the performance of such structures. A glass/epoxy material system and Nitinol, ribbon-type actuators were selected for the SMAHC fabrication and testing program. The Nitinol alloy was tested for its transformation and mechanical properties, which were used to form a thermoelastic constitutive model of the actuator material in a constrained recovery configuration. Actuator material was acquired in a ribbon form and tested for its mechanical properties.

A SMAHC laminate was manufactured from the glass/epoxy material system with a quasi-isotropic lamination and Nitinol actuators, with a prestrain of 4%, embedded in discrete 0.011 m (0.45 in) strips in four (0°) of 16 layers. Beam specimens were machined from the laminate sharing the centerline of the embedded SMA strips. The overall volume fraction of the SMA is approximately 14%. Experiments were conducted on a beam specimen in a base acceleration configuration with resistive heating controlled by thermocouple measurement. Frequency response functions and power spectral densities of the beam response were recorded with random base acceleration at ambient and at elevated temperatures from 32.22°C (90°F) to 121.11°C (250°F) in 5.56°C (10°F) increments.

A rather large thermal post-buckling deflection was noted at slightly elevated temperatures below the austenite start temperature A_s . At temperatures above A_s , the thermal post-buckling deflection was eliminated and enormous stiffening effects were observed. The fundamental frequency of the beam was shifted by a factor of 5.3 at 121.11°C (250°F), relative to the ambient temperature resonance. The maximum RMS displacement response attenuation of a factor of 6.4 was achieved at a temperature of 71.11°C (160°F) rather than at the maximum temperature. This was apparently caused by enhanced damping due to stress induced martensitic transformation hysteresis. Nonetheless, similar attenuations of around a factor of 5 were achieved at higher temperatures.

A model of the SMAHC beam specimen was developed using measured temperature dependent properties for the Nitinol and nominal, ambient properties for the glass/epoxy matrix. Comparisons between predicted and measured dynamic responses show excellent agreement at ambient temperature with some discrepancy at elevated temperatures. The discrepancy diminishes with increasing temperature. It is expected that this effect is mainly attributable to underestimation of the longitudinal matrix coefficient of thermal expansion and overestimation of the elevated temperature matrix moduli. Work is currently in progress to obtain appropriate matrix material properties and perform a rigorous correlation with experimental results.

8. ACKNOWLEDGMENTS

The author gratefully acknowledges the assistance of Cynthia Lach, R. Keith Bird, Roberto Cano, Hoa Luong, Louis Simmons, Howard Jones, Jeff Pierro, Scott Wallace (NASA Langley Research Center), Joel Alexa, Stewart Walker (Analytical Services and Materials), and Jerry Draper (Lockheed Martin Astronautics) for their help in alloy characterization, actuator prestraining, hybrid composite fabrication and machining, and vibration testing.

REFERENCES

1. Tanaka, K. and Nagaki, S.: "A Thermomechanical Description of Materials with Internal Variables in the Process of Phase Transformation," *Ingenieur-Archiv*, 51:287–299, 1982.
2. Liang, C. and Rogers, C. A.: "One-Dimensional Thermomechanical Constitutive Relations for Shape Memory Materials," *Journal of Intelligent Material Systems and Structures*, 1:207–235, 1990.
3. Brinson, L. C.: "One Dimensional Constitutive Behavior of Shape Memory Alloys: Thermomechanical Derivation with Non-Constant Material Functions," *Journal of Intelligent Material Systems and Structures*, 4(2):229–242, 1993.

4. Boyd, J. G. and Lagoudas, D. C.: "A Thermodynamical Constitutive Model for Shape Memory Materials – Part I: The Monolithic Shape Memory Alloy", *Int. J. of Plasticity*, 12:805–842, 1996.
5. Cross, W. B.; Kariotis, A. H.; and Stimler, F. J.: "Nitinol Characterization Study," NASA CR-1433, 1969.
6. Jackson, C. M.; Wagner, H. J.; and Wasilewski, R. J.: "55–Nitinol The Alloy with a Memory: Its Physical Metallurgy, Properties, and Applications," NASA SP-5110, 1972.
7. Otsuka, K. and Wayman, C. M. (Editors): *Shape Memory Materials*, Cambridge University Press, Cambridge, CB2 2RU, UK, 1998.
8. Birman, V.: "Review of Mechanics of Shape Memory Alloy Structures," *Applied Mechanics Reviews*, 50(11):629–645, 1997.
9. Buehler, W. J. and Wiley, R. C.: "Nickel-Base Alloys," U. S. Patent 3,174,851, 23 March 1965.
10. Buehler, W. J. and Wang, F. E.: "A Summary of Recent Research on the Nitinol Alloys and Their Potential Application in Ocean Engineering," *Ocean Engineering*, 1:105–120, 1968.
11. Wayman, C. M. and Shimizu, K.: "The Shape Memory ("Marmem") Effect in Alloys," *Metal Science Journal*, 6:175–183, 1972.
12. Wayman, C. M.: "Some Applications of Shape-Memory Alloys," *Journal of Metals*, pp. 129–137, June 1980.
13. Otsuka, K. and Shimizu, K.: "Pseudoelasticity and Shape Memory Effects in Alloys," *International Metals Reviews*, 31(3):93–114, 1986.
14. Rogers, C. A. and Robertshaw, H. H.: "Shape Memory Alloy Reinforced Composites," *Engineering Science Preprints* 25, Society of Engineering Science, Inc., ESP25.8027, 1988.
15. Rogers, C. A.: "Active Vibration and Structural Acoustic Control of Shape Memory Alloy Hybrid Composites: Experimental Results", *J. of the Acoustical Society of America*, 88(6):2803–2811, 1990.
16. Baz, A.; Imam, K.; and McCoy, J.: "Active Vibration Control of Flexible Beams Using Shape Memory Actuators", *Journal of Sound and Vibration*, 140(3):437–456, 1990.
17. Srinivasan, A. V.; Cutts, D. G.; and Schetky, L. M.: "Thermal and Mechanical Considerations in Using Shape Memory Alloys to Control Vibrations in Flexible Structures", *Metallurgical Transactions A*, 22A:623–627, 1991.
18. Chaudhry, Z. and Rogers, C. A.: "Bending and Shape Control of Beams Using SMA Actuators", *J. of Intell. Syst. and Struct.*, 2:581–602, 1991.
19. Maclean, B. J.; Patterson, G. J.; and Misra, M. S.: "Modeling of a Shape Memory Integrated Actuator for Vibration Control of Large Space Structures", *J. of Intell. Mater. Syst. and Struct.*, 2:72–94, 1991.
20. Rogers, C. A.; Liang, C.; and Jia, J.: "Structural Modification of Simply-Supported Laminated Plates Using Embedded Shape Memory Alloy Fibers", *Computers and Structures*, 38(5/6):569–580, 1991.
21. Liang, C.; Rogers, C. A.; and Fuller, C. R.: "Acoustic Transmission and Radiation Analysis of Adaptive Shape Memory Alloy Reinforced Laminated Plates", *Journal of Sound and Vibration*, 145(1):23–41, 1991.
22. Zhong, Z. W.; Chen, R. R.; Mei, C.; and Pates, C. S.: "Buckling and Postbuckling of Shape Memory Alloy Fiber-Reinforced Composite Plates", *Symposium on Buckling and Postbuckling of Composite Structures*, ASME AD-Vol. 41/PVP-Vol. 293:115–132, 1994.
23. Turner, T. L.; Zhong, Z. W.; and Mei, C.: "Finite Element Analysis of the Random Response Suppression of Composite Panels at Elevated Temperatures Using Shape Memory Alloy Fibers," *Proceedings of the 35th Structures, Structural Dynamics and Materials Conference*, Hilton Head, SC, April 18–21, pp. 136–146, 1994.
24. Ro, J. and Baz, A.: "Nitinol-Reinforced Plates: Part I. Thermal Characteristics", *Composites Engineering*, 5(1):61–75, 1995.
25. Ro, J. and Baz, A.: "Nitinol-Reinforced Plates: Part II. Static and Buckling Characteristics", *Composites Engineering*, 5(1):77–90, 1995.
26. Ro, J. and Baz, A.: "Nitinol-Reinforced Plates: Part III. Dynamic Characteristics", *Composites Engineering*, 5(1):91–106, 1995.
27. Birman, V.: "Stability of Functionally Graded Shape Memory Alloy Sandwich Panels", *Smart Materials and Structures*, 6:278–286, 1997.
28. Boyd, J. G. and Lagoudas, D. C.: "A Thermodynamical Constitutive Model for Shape Memory Materials – Part II: The SMA Composite Material", *Int. J. of Plasticity*, 12(7):843–873, 1996.
29. Birman, V.: "Micromechanics of Composites with Shape Memory Alloy Fibers in Uniform Thermal Fields", *AIAA Journal*, 34(9):1905–1912, 1996.
30. Turner, T. L.: "A New Thermoelastic Model for Analysis of Shape Memory Alloy Hybrid Composites", *Accepted for publication in the J. of Intell. Matl. Syst. and Struct.*, 2000.

31. Draper, J. L.: “Thermomechanical Characterization Report for NiTi Shape Memory Alloy Ribbon”, Contractor Report, Lockheed Martin Astronautics, Denver, CO, 1997.

Table 1. Material properties for glass/epoxy and Nitinol.

<u>Glass/Epoxy</u>		<u>Nitinol</u>	
E_1	51.02 GPa (7.4 Msi)	σ_r	from figure 3
E_2	23.44 GPa (3.4 Msi)	E	from table 2
G_{12}	11.03 GPa (1.6 Msi)	ν	0.3
ν_{12}	0.28	ρ	5720 kg/m ³ (0.535×10 ⁻³ lbf s ² /in. ⁴)
ρ	2031.8 kg/m ³ (0.19×10 ⁻³ lb s ² /in. ⁴)	α_{1a}	6.61×10 ⁻⁶ /°C (3.67×10 ⁻⁶ /°F), $T < A_s$ from equation 2, $T \geq A_s$
α_1	5.4×10 ⁻⁶ /°C (3.5×10 ⁻⁶ /°F)	α_{2a}	6.61×10 ⁻⁶ /°C (3.67×10 ⁻⁶ /°F), $T < A_s$ 11.0×10 ⁻⁶ /°C (6.11×10 ⁻⁶ /°F), $T > A_f$ interpolation, $A_s \leq T \leq A_f$
α_2	30.6×10 ⁻⁶ /°C (11.4×10 ⁻⁶ /°F)		

Table 2. Summary of Nitinol characterization tests.

Sample	Prestrain, %	# of Cycles	Maximum Stress, MPa		Young's Modulus, GPa	
			Initial	Final	120°C	Ambient
1	1.99	50	429.42	296.00	55.50	22.75
2	3.08	50	532.98	363.30	62.47	25.10
3	3.07	10	517.13	396.32	56.06	24.41
4	4.00	50	586.28	412.67	55.64	24.34
5	3.95	10	579.25	442.11	55.92	24.20
6	N/A	0	N/A	N/A	59.78	14.41

Table 3. Summary of RMS displacements at 0.254 m (10 in) location and modal parameters versus temperature.

Temp. °C	RMS Displ. m	f_1 Hz	ζ_1 %	f_3 Hz	ζ_3 %	Temp. °C	RMS Displ. m	f_1 Hz	ζ_1 %	f_3 Hz	ζ_3 %
23	0.322e-3	26.4	0.89	160.3	0.95	87.78	0.063e-3	130.9	0.14	—	—
—	—	—	—	—	—	93.33	0.062e-3	134.0	0.14	—	—
60	0.15e-3	83.1	0.10	279.3	0.45	98.89	0.066e-3	136.0	0.11	—	—
65.56	0.11e-3	94.4	0.13	309.4		104.44	0.067e-3	137.6	0.11	—	—
71.11	0.05e-3	107.0	0.50	342.7	0.16	110	0.073e-3	139.2	0.10	—	—
76.67	0.063e-3	118.3	0.19	372.5	0.28	115.56	0.072e-3	139.7	0.10	—	—
82.22	0.068e-3	126.7	0.15	—	—	121.11	0.067e-3	140.0	0.09	—	—

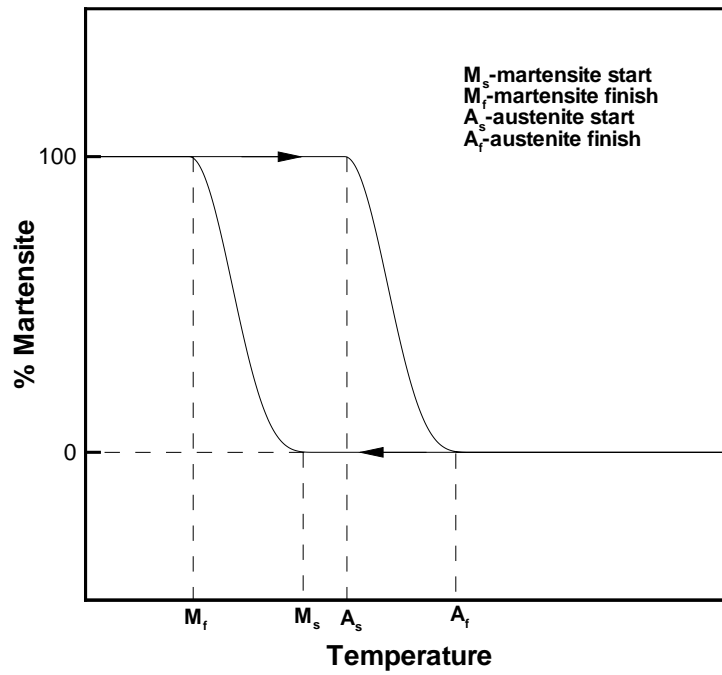


Figure 1. Schematic of the martensitic and reverse transformation temperatures, after Liang and Rogers².

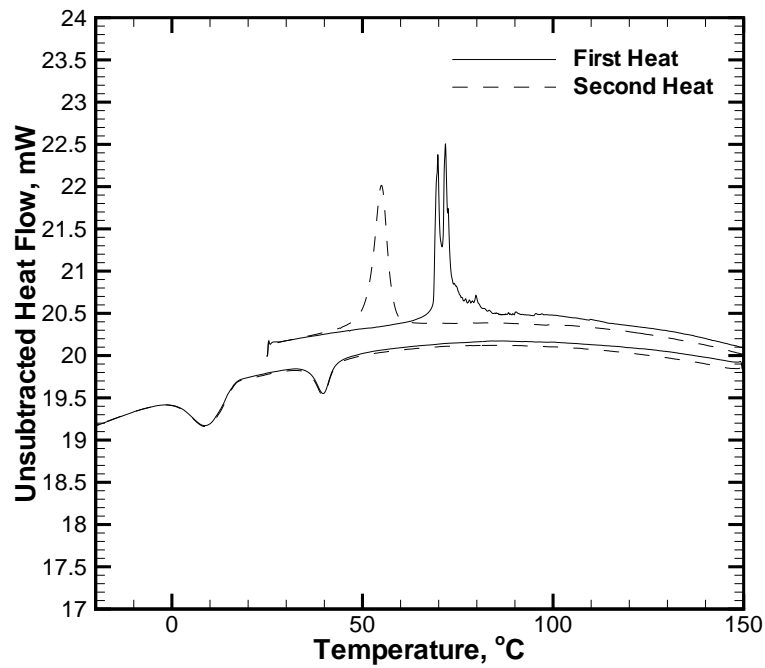


Figure 2. DSC signatures for first- and second-heat of as-received material.

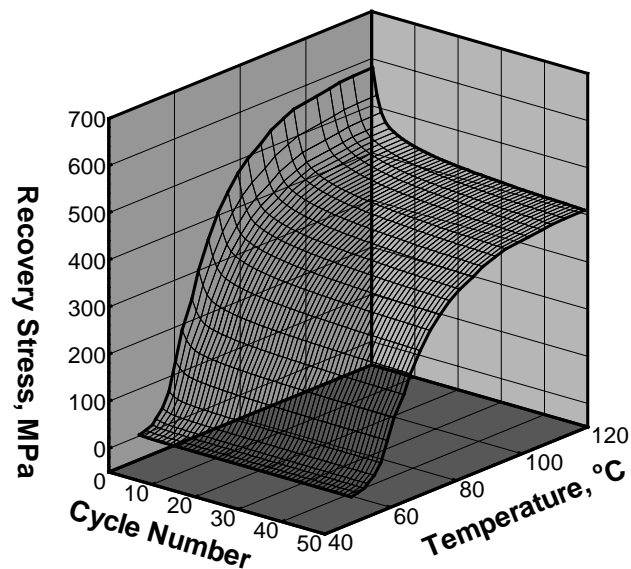


Figure 3. Recovery stress versus thermal cycle number temperature for sample with 4% prestrain.

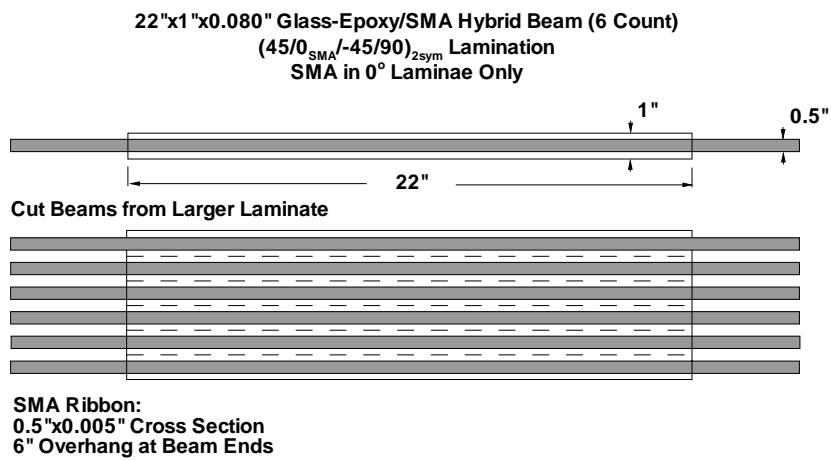


Figure 4. Schematic of beam specimens cut from a SMA hybrid composite laminate.

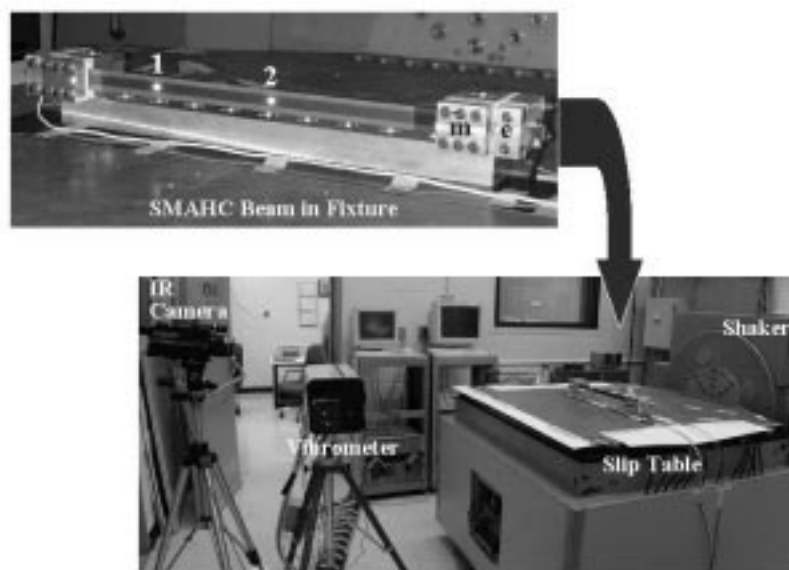


Figure 5. Pictures of the SMAHC beam supported in a clamping fixture and mounted to a slip table of an electromechanical shaker system.

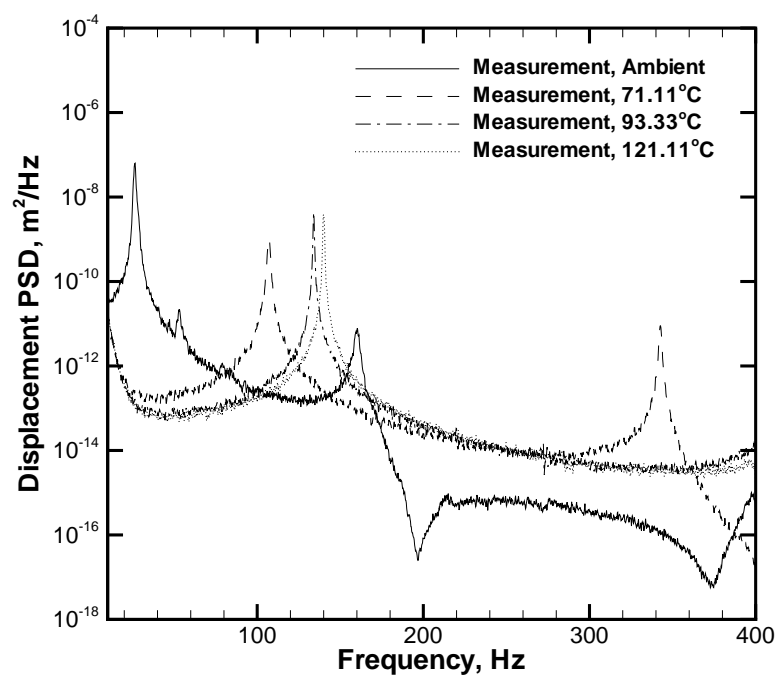


Figure 6. Measured displacement PSDs of the SMAHC beam for location 2 at four temperatures.

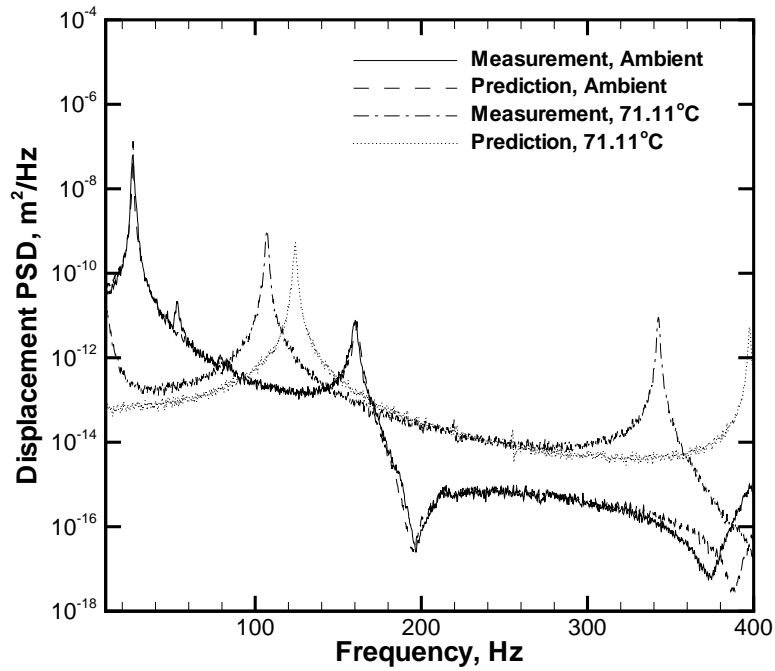


Figure 7. Comparison of measured and predicted displacement PSDs for location 2 at ambient temperature and 71.11°C (160°F).

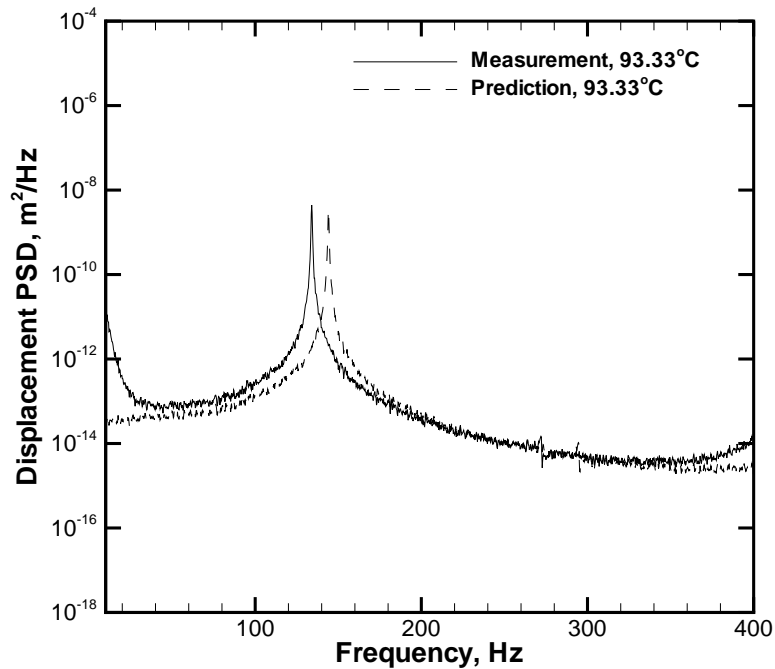


Figure 8. Comparison of measured and predicted displacement PSDs for location 2 at 93.33°C (200°F).